Summer precipitation variability over Southeastern South America in a global warming scenario

C. Junquas · C. Vera · L. Li · H. Le Treut

Abstract December–January–February (DJF) rainfall variability in southeastern South America (SESA) is studied in 18 coupled general circulation models from the WCRP/CMIP3 dataset, for present climate and the SRES-A1B climate change scenario. The analysis is made in terms of properties of the first leading pattern of rainfall variability in the region, characterized by a dipole-like structure with centers of action in the SESA and South Atlantic Convergence Zone (SACZ) regions. The study was performed to address two issues: how rainfall variability in SESA would change in a future climate and how much of that change explains the projected increasing trends in the summer mean rainfall in SESA identified in previous works. Positive (negative) dipole events were identified as those DJF seasons with above (below) normal rainfall in SESA and below (above) normal rainfall in the SACZ region. Results obtained from the multi-model ensemble confirm that future rainfall variability in SESA has a strong projection on the changes of seasonal dipole pattern activity, associated with an increase of the frequency of the positive phase. In addition, the frequency increase of positive dipole phase in the twenty first century seems to be associated with an increase of both frequency and intensity of positive SST anomalies in the equatorial Pacific, and with a Rossby wave train-like anomaly pattern linking that ocean basin to South America, which regionally induces favorable conditions for moisture transport convergence and rainfall increase in SESA.

1 Introduction

It has been a challenge for the international scientific community to understand future climate changes associated to greenhouse gas increase, particularly at regional scales. The World Climate Research Program-Coupled Model Intercomparison Project (WCRP-CMIP3) Experiment has provided the most comprehensive scenarios for future climate change studies, so far. In particular, the multi-model projection for the twenty first century indicates general increases of summer precipitation in the tropical monsoonal areas and decreases in the subtropics. However, the region of southeastern South America (SESA) is one of the few subtropical regions where projected summer rainfall increases significantly by the end of the twenty first century (IPCC 2007). SESA includes the La Plata basin, where an increasing trend of the annual rainfall has already been identified during the twentieth century, with a rainfall increase between 20 and 30% (Giorgi 2002). La Plata basin is the second largest basin in South America, being a region with dense populations and local economies strongly depending on agricultural activities and hydro-electricity generation. Therefore, assessing projected precipitation changes in this region is an important and considerable challenge.

During summer, rainfall in SESA is strongly linked to the South American monsoon system (SAMS) (e.g., Vera et al.

C. Junquas · L. Li · H. Le Treut
Laboratoire de Météorologie Dynamique, Institut Pierre Simon Laplace, Ecole Polytechnique, UPMC/CNRS, Paris, France

C. Junquas (✉) · C. Vera
Centro de Investigaciones del Mar y la Atmósfera (CIMA), DCAO/FCEyN, UMI-IFAECI CNRS-CONICET-UBA, Buenos Aires, Argentina
e-mail: junquas@cima.fcen.uba.ar

2006a; Marengo et al. 2010). One of the distinctive features of SAMS is represented by the South American Convergence Zone (SACZ), a southeastward band of cloudiness and precipitation extending from southern Amazon towards southeastern Brazil and the surrounding Atlantic Ocean (e.g., Kodama 1992). In addition, a considerable portion of the moisture present in SESA comes from the Amazon basin, transported by the South American low-level jet (SALLJ) that is located east of the Andes, and it is a crucial component of the atmospheric water cycle in the region, (e.g., Berbery and Barros 2002). The SALLJ is considered to close off the South Atlantic subtropical anticyclone located to the east of the continent (Rodwell and Hoskins 2001).

Summer rainfall variability in SESA is also influenced by SACZ and moisture transport variability at a wide range of timescales (Vera et al. 2006a). The leading pattern of summer rainfall variability in SESA on interannual timescales is characterized by a dipole-like structure with rainfall anomaly centers of opposite signs located at both SESA and the SACZ regions (e.g., Doyle and Barros 2002). Nogués-Paegle and Mo (1997) identified a similar seesaw-like pattern in the variability of OLR anomalies filtered on intraseasonal timescales. Such pattern tends to promote above-normal rainfall in SESA and below-normal rainfall in the SACZ region, or vice versa. Changes in the strength and direction of the SALLJ controlling the moisture transport from the Amazon basin into SESA, have also been identified at both intraseasonal (e.g., Nogués-Paegle and Mo 1997; Li and Le Treut 1999) and interannual timescales (Doyle and Barros 2002). Strong (weak) SALLJ events are associated to a westward (eastward) shift of the South Atlantic subtropical high, leading to an increase (decrease) of moisture transport and convective activity in SESA and to a weakened (enhanced) SACZ (e.g., Nogués-Paegle and Mo 1997). In addition, weakened (enhanced) diabatic heat release by the SACZ has been linked to a decrease (increase) of the compensating subsidence over SESA (e.g., Gandu and Silva Dias 1998; Robertson and Mechoso 2000; Cerne and Vera 2010).

It has been recognized that climate variability in SESA is remotely influenced by sea surface temperature (SST) anomalies in the tropical Pacific Ocean associated to El Niño Southern Oscillation (ENSO; e.g., Paegle and Mo 2002 and references therein). ENSO influence is exerted through a Rossby wave train extended between the tropical Pacific Ocean and South America along an arch trajectory. During warm ENSO phase, the wave train induces a cyclonic low-level circulation anomaly at the extratropical regions of South America, and an anticyclonic low-level circulation anomaly in the tropics (e.g., Grimm et al. 2000). These circulation anomalies lead to a convergence of

moisture transport anomalies and precipitation increase over SESA and a divergence of moisture transport anomalies over the SACZ region. In addition, variability of the rainfall anomaly dipole pattern has been linked to SST anomalies in the South Atlantic Ocean (e.g., Robertson and Mechoso 2000; Doyle and Barros 2002). In particular, positive phase of the dipole pattern that corresponds to rainfall above normal in the SESA and below normal in the SACZ region has been associated to warm SST anomalies in the western subtropical South Atlantic (WSSA; Doyle and Barros 2002).

From the above-mentioned studies, it is evident that summer rainfall variability in SESA results from complex physical processes involving both regional and remote phenomena. But how is its future evolution going to be under a global warming context? How much of the projected changes in the summer mean rainfall is accounted by changes in the rainfall year-to-year variability? Considering the major relevance of the dipole pattern on summer rainfall variability in SESA, as described by other studies, the motivation of this work is thus to answer these questions quantifying future rainfall variability in the region in terms of properties of the dipole structure associated to the leading pattern of regional rainfall variability. Emphasis is made in studying the physical processes underlying variations of the dipole pattern in a global warming scenario associated to an increase of greenhouse gases.

Our results will confirm, through the analysis of the behavior of the dipole pattern in a GHG-increase scenario as depicted by the multi-model ensemble that the increasing trend of summer precipitation projected in the SESA region seems to be associated to an increase of the frequency of the positive phase of the dipole that induces positive rainfall anomalies in SESA. Furthermore, such an increase in the frequency of those dipole events seems linked to a differential warming of the tropical Pacific Ocean in the context of a GHG-increase scenario.

The paper is organized as follows: main features of the data set and climate models considered are presented in Sect. 2, which also includes a methodology discussion. In Sect. 3, the ability of the climate models in representing the dipole pattern is discussed as well as the changes of dipole activity depicted by the multi-model ensemble. Section 3 also includes an analysis of the criteria that has been followed to select the most suitable multi-model ensemble to study the projected changes of the summer rainfall dipole variability. The dynamics associated to future changes in the dipole pattern and in particular its relationship to SST changes in the tropical oceans, are analyzed in Sect. 4. Finally, we summarize and conclude in Sect. 5.

2 Data and methodology

Monthly means of rainfall, SST and a few tropospheric variables were obtained from the set of simulations of 18 coupled general circulation models (CGCMs; Table 1) of the WCRP/CMIP3 multi-model dataset computed for the IPCC-AR4 Report (Meehl et al. 2007). The 18 models were chosen according to the availability of variables needed for the study. The simulations of the "climate of the twentieth century experiment" (20C3M) are used to describe the climate conditions for the period 1979–1999, while the simulations for the twenty first century based on the scenario SRES-A1B are considered to describe future climate change conditions. SRES-A1B corresponds to a continuous increase of the CO2 concentration over the twenty first century until a level of 720 ppm by 2100 (Nakicenovic et al. 2000). It has been extensively used in the literature as it represents a midrange future scenario. Detailed documentation about the multi-model dataset can be found at http://www-pcmdi.llnl.gov/ipcc/model documentation/ipccmodeldocumentation.php. In addition, monthly mean rainfall fields from the Climate Prediction Center (CPC) Merged Analysis of Rainfall (CMAP) dataset (Xie and Arkin 1997) are used to describe the mean and variability conditions observed in the rainfall between 1979 and 1999.

An empirical orthogonal function (EOF) analysis of the seasonal (December–January–February; DJF) rainfall anomalies was made over South America to describe the year-to-year summer rainfall variability. The leading pattern displays a dipole-like structure with rainfall anomalies of opposite sign over SESA and the SACZ region, respectively (Fig. 1a). In order to focus the study over SESA, the EOF analysis domain was reduced at 39°–16°S and 64°–31°W. The resulting leading mode (EOF1) also represents a dipole-like structure (Fig. 1b), and its corresponding time series (PC1) exhibits a correlation of 0.69 with that associated to the leading pattern resulted from the continental-scale domain. Moreover, EOF1 pattern is similar to the dipolar structure described by Doyle and Barros (2002) and more recently, by Grimm and Zilli (2009), both of them considering different regions and periods. The rainfall dipole identified in the SESA domain (Fig. 1b) is then considered in the rest of the paper to represent the summer rainfall variability in the region.

3 Multi-model ensemble and rainfall in SESA

Extracting the most useful information and estimating uncertainties from a large number of climate models and simulations is still a challenge. In particular, for some regions, eliminating models that poorly represent present-day climate or exhibit incoherent physical behavior in a future climate, results often in a spread decrease of the multi-model ensemble (Knutti 2010 and references therein).

Previous works have shown that most of WCRP-CMIP3 models are able to describe the main features associated to South America summer climate, although they still exhibit considerable dispersion in quantifying mean and variability of summer rainfall in the region (e.g., Vera et al. 2006b; Vera and Silvestri 2009).

In the following sections, a detailed analysis of the ability of the 18 models in depicting the features associated with the leading pattern of rainfall variability is presented. We will show, furthermore, that the most suitable models to study the changes of the DJF rainfall dipole and its physical processes in the future are those showing: (1) ability to represent the rainfall dipole pattern in the present as in the future climate, (2) coherence in projecting positive rainfall changes in SESA by the end of the twenty first century, and (3) a coherent behavior of the future evolution of the dipole. As it is explained below, nine of the eighteen considered models fulfill the required criteria.

3.1 Representation of the DJF rainfall dipole

The ability of the models in representing the space–time features of the observed leading modes of rainfall inter-annual variability is firstly assessed. The EOF analysis was applied to the DJF rainfall anomalies of the 18 models for the periods 1979–1999 and 2001–2098 respectively. A comparison between the EOF1 obtained from observations (Fig. 1b) and those depicted by the models for the end of the twentieth century (Fig. 2) reveals that 14 models represent a dipole-like structure similar to that observed, while 4 models (GISS-eh, GISS-er, IPSL and MPI) having strong limitations to represent it. Figure 2 also shows that a common model bias detected for the late twentieth century, is that the simulated centers of action of the dipole pattern are shifted northeastward with respect to the observed counterparts. Table 2 shows the spatial correlations between the EOF1 obtained from CMAP and those obtained from the model simulations. They are statistically significant for most of the models with exception of GISS-er, MPI, and IPSL. It was found that these four models exhibits a dipole-like structure in association to their corresponding EOF2, meaning that although these models can reproduce such pattern, it is not the dominant one. Figure 2 also shows that GISS-eh model exhibits a subtropical center of action of the corresponding EOF1 located off the coast. EOF1 was also computed from the model simulations for the twenty first century (2001–2098) (not shown) and most models are also able to represent the dipole-like structure for this period. The exception is GISS-AOM, which exhibits an EOF1 that is not significantly associated

Table 1 Models used in the study

Acronym	Model name	Institutes (Country)	Resolutions (°lat × °lon)	References
CCCMA T47	CGCM3.1(T47)	Canadian Center for Climate Modeling and Analysis (Canada)	Atm: T47 (~2.8° × 2.8°) Ocn: 1.9° × 1.9°	Flato (2005)
CCCMA T63	CGCM3.1(T63)	Canadian Center for Climate Modeling and Analysis (Canada)	Atm: T63 (~1.9° × 1.9°) Ocn: 0.9° × 1.4°	Flato (2005)
CNRM	CNRM-CM3	Météo-France/Centre National de Recherches Météorologiques (France)	Atm: T63 (~1.9° × 1.9°) Ocn: 0.5°–2° × 2°	Salas-Melia et al. (2005)
CSIRO	CSIRO-MK3.0	CSIRO Atmospheric Research (Australia)	Atm: T63 (~1.9° × 1.9°) Ocn: 0.8° × 1.9°	Gordon et al. (2002)
GFDL2.0	GFDL-CM2.0	US Dept. of Commerce/NOAA/Geophysical Fluid Dynamics Laboratory (USA)	Atm: 2° × 2.5° Ocn: 0.3–1° × 1°	Delworth et al. (2006)
GFDL2.1	GFDL-CM2.1	US Dept. of Commerce/NOAA/Geophysical Fluid Dynamics Laboratory (USA)	Atm: 2° × 2.5° Ocn: 0.3–1° × 1°	Delworth et al. (2006)
GISS AOM	GISS-AOM	NASA/Goddard Institute for Space Studies (USA)	Atm: 3° × 4° Ocn: 3° × 4°	Russell (2005)
GISS-EH	GISS-EH	NASA/Goddard Institute for Space Studies (USA)	Atm: 4° × 5° Ocn: 2° × 2°	Schmidt et al. (2006)
GISS-ER	GISS-ER	NASA/Goddard Institute for Space Studies (USA)	Atm: 4° × 5° Ocn: 4° × 5°	Schmidt et al. (2006)
INM	INM-CM3.0	Institute for Numerical Mathematics (Russia)	Atm: 5° × 4° Ocn: 2° × 2.5°	Volodin and Diansky (2004)
IPSL	IPSL-CM4	Institut Pierre Simon Laplace (France)	Atm: 2.5° × 3.75° Ocn: 2° × 2°	Marti et al. (2005)
MIROC hires	MIROC3.2(hires)	Cent. for Clim. Sys. Res, Univ of Tokyo, Nat. Inst. for Envir. Studies & Frontier Res. Cent. For Global Change (Japan)	Atm: T101 (~1.1° × 1.1°) Ocn: 0.2° × 0.3°	Hasumi et al. (2004)
MIROC medres	MIROC3.2(medres)	Cent. for Clim. Sys. Res, Univ of Tokyo, Nat. Inst. for Envir. Studies & Frontier Res. Cent. For Global Change (Japan)	Atm: T42 (~2.8° × 2.8°) Ocn: 0.5°–1.4° × 1.4°	Hasumi et al. (2004)
MIUB	ECHO-G	Meteorological Institute of the University of Bonn (Germany)	Atm: T30 (3.9° × 3.9°) Ocn: 0.5°–2.8° × 2.8°	Min et al. (2005)
MPI	ECHAM5/MPI-OM	Max Planck Institute for Meteorology (Germany)	Atm: T63 (~1.9° × 1.9°) Ocn: 1.5° × 1.5°	Jungclaus et al. (2006)
MRI	MRI-CGCM2.3.2	Meteorological Research Institute (Japan)	Atm: T42 (~2.8° × 2.8°) Ocn: 0.5 ~ 2° × 2.5°	Yukimoto et al. (2006)
UKMO hadCM3	UKMO HadCM3	Hadley Centre for Climate Prediction and Research/Met Office (UK)	Atm: 2.5° × 3.75° Ocn: 1.25° × 1.25°	Gordon et al. (2000)
UKMO hadGEM1	UKMO HadGEM1	Hadley Centre for Climate Prediction and Research/Met Office (UK)	Atm: ~1.3° × 1.9° Ocn: 0.3°–1° × 1°	Johns et al. (2006)

to the observed one (Table 2). In essence, 13 of the 18 models are able to represent the rainfall dipole as the leading mode in a present period as in the future projections. The 5 other models (GISS-AOM, GISS-eh, GISS-er, IPSL and MPI) show limited ability to represent it as the leading pattern of rainfall variability and they should

Fig. 1 Leading mode of the
Empirical Orthogonal Function
(EOF1) of December–January–
February (DJF) rainfall
anomalies for the 1979–1999
period, from the CMAP dataset
over two different domains of
South America, explaining
a 21% and **b** 19% of the total
variance, respectively. *Color
scale* interval is 0.2 non-
dimensional units. *Black
contour* indicates the 0 level
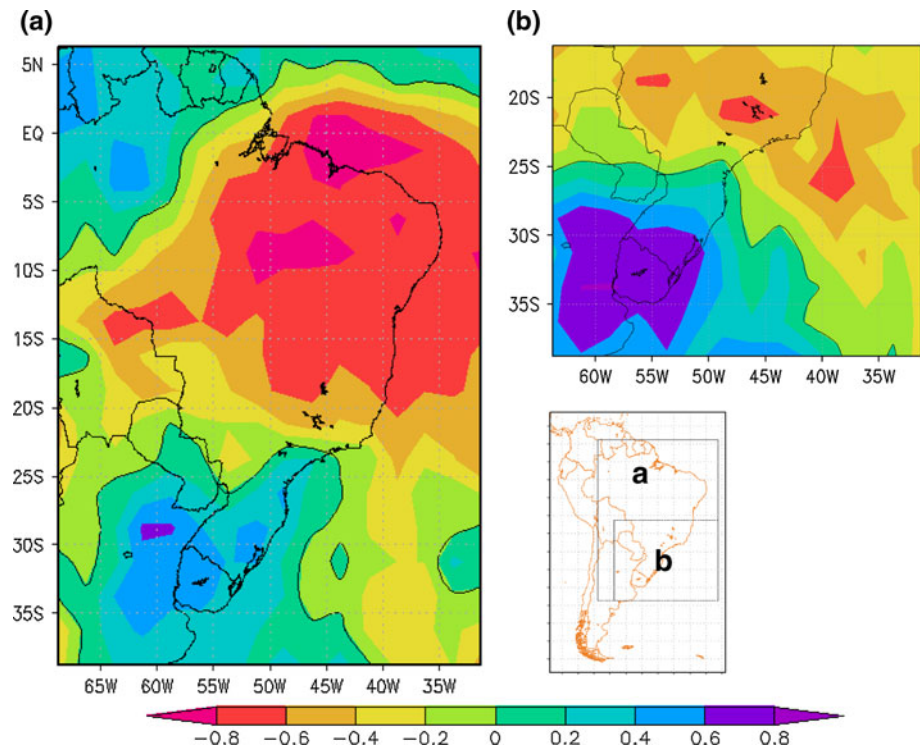
not be part of a model ensemble used to study the dipole
evolution.

An analysis of the variance percentage explained by the
EOF1 computed over the end of the twentieth century
(Table 2), reveals that the pattern obtained from CMAP
data explains 19% of variance while for most of the
models, it explains between 20 and 40%. A decrease of the
variance explained by EOF1 is found, however, for the
majority of the models when the pattern is computed over
the whole twenty first century period, ranging those per-
centages between 18 and 30% (Table 2). Nevertheless, it
seems that models in average tend to overestimate in some
extent the activity of EOF1.

### 3.2 Projected changes of DJF mean rainfall

Changes of DJF mean rainfall, simulated by the 18 climate
models from 1979–1999 to 2079–2099, are depicted in
Fig. 3. As it was mentioned in Introduction, the IPCC-AR4
report pointed out a significant increase of the DJF rainfall
in SESA from a 23-model ensemble mean, in which at
around 14 of the models agree in a positive rainfall change
in that area (Christensen et al. 2007). Figure 3 shows that
among the 18 models considered in this study, 12 of them
show that rainfall changes over the subtropical regions are
associated to changes of opposite sign in the tropics, par-
ticularly over the SACZ region. To confirm the latter, an
EOF analysis was performed over the 18 rainfall difference

maps displayed in Fig. 3, and the resulting leading mode
that explains 36% of the variance clearly exhibits the
seesaw pattern between SESA and the SACZ region (not
shown). Therefore, the dipole-like pattern not only appears
in most of the models as the leading mode of summer
rainfall variability, but it seems also to be the spatial
structure that characterizes the most common response
signal among the models in a global warming scenario.
Moreover, 9 of those 12 models (indicated with red labels
in Fig. 3) project a precipitation increase in SESA and a
decrease in the SACZ region, which constitutes the dom-
inant structure for rainfall projection in SESA. The
remaining 3 models (CNRM, IPSL, UKMO-hadGEM1)
project the opposite change that is rainfall decrease in
SESA and increase in the SACZ. These results are con-
sistent with Vera et al. (2006b), who found an increase of
the DJF rainfall in SESA in most of the models, but with
changes less consistent in the SACZ region.

3.3 DJF rainfall dipole activity in a climate change scenario

In order to explore the evolution of the rainfall dipole
pattern along the twenty first century, EOF1 events were
identified as those years when PC1 is larger (smaller) than
1 (−1) standard deviation of its interannual variability.
These years represent the positive (negative) phases of
large amplitude of the dipole and they are associated to

Fig. 2 EOF1 of DJF rainfall for the 1979–1999 period, from the 18 WCRP/CMIP3 models (see the list in Table 1). *Color scale* interval is 0.2 non-dimensional units. *Black contour* indicates the 0 level. The 9 models identified in Sect. 3.2 are marked in *red*
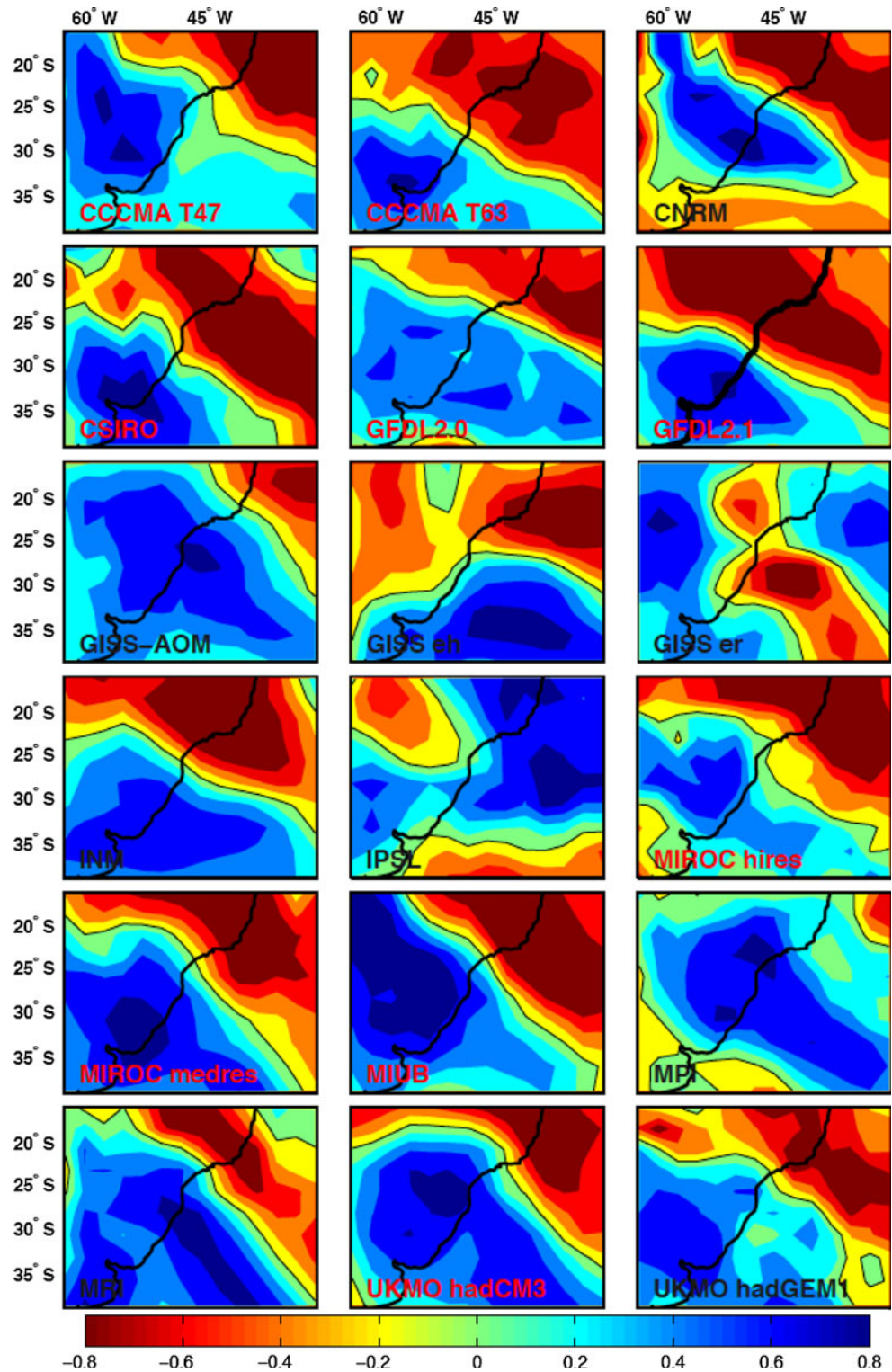
above- (below-) normal rainfall in SESA. Such events are hereafter called positive (negative) EOF1 events. As an example, Fig. 4 displays the time series of PC1 and the corresponding EOF1 events (red and blue dots) for two models with different behavior. An increasing trend is

observed in PC1 values for GFDL2.0 leading to a progressive frequency increase of positive EOF1 events and a frequency decrease of negative EOF1 events, with a reduction of its amplitude (Fig. 4a). On the contrary, IPSL shows a long-term negative trend in the corresponding PC1

Table 2 List of EOF1 explained variances and spatial correlation between each model EOF1 and CMAP EOF1

Model	EOF1 explained variances (%)		Correlation [EOF1(model) and EOF1(CMAP)]	
	1979–1999	2001–2098	1979–1999	2001–2098
CCCMA T47	25	24	0.5984	0.7015
CCCMA T63	23	25	0.8948	0.8681
CNRM	26	22	0.3504	0.5416
CSIRO	31	22	0.8315	0.8924
GFDL2.0	21	18	0.5962	0.6548
GFDL2.1	31	25	0.8708	0.8395
GISS AOM	26	26	0.3040	**0.1994**
GISS-EH	25	26	0.4605	0.6908
GISS-ER	20	19	**0.0819**	0.5495
INM	32	23	0.8208	0.8064
IPSL	26	19	**−0.2143**	0.3707
MIROC hires	26	20	0.6694	0.8183
MIROC medres	32	23	0.8336	0.7278
MIUB	41	30	0.6520	0.4536
MPI	22	21	**−0.0779**	0.4550
MRI	28	23	0.7258	0.3613
UKMO hadCM3	32	30	0.5984	0.7897
UKMO hadGEM1	23	23	0.8204	0.8738
Total mean	27.22	23.28	0.5454	0.6441
9-model mean	29.11	24.11	0.7272	0.7495

Correlation values statistically no significant at 95% are boldface

evolution with no significant changes in the corresponding interannual variability (Fig. 4b).

The evolution of both positive and negative EOF1 events was analyzed by contrasting two periods: 2001–2049 and 2050–2098, which are the first and second parts of the twenty first century, respectively. Changes in the frequency of both positive and negative EOF1 events are represented for each of the models in Fig. 5 and those for the multi-model ensemble mean in Fig. 6. Left and right bars represent the number of EOF1 events during the first and the second half of the twenty first century, respectively. Figure 5 shows that 10 models exhibit by the second half of the twenty first century a common behavior characterized by a frequency increase of positive EOF1 events and a frequency decrease of negative EOF1 events. Among these 10 models, the MPI model is included that should not be considered based on the previous discussion in Sect. 3.1. The remaining 9 models (indicated with a red star in Fig. 5) are exactly the same ones identified in Sect. 3.2. The 18-model ensemble shows, in average, a similar behavior (Fig. 6), although the mean changes in the frequency of EOF1 events are smaller than the inter-model variability and these changes present a very-low statistical significance. The statistical significance, from a Student's t test for the 9-model ensemble, reaches easily to the 99% of confidence level. This is clearly larger than that obtained

for the 18-model ensemble (Fig. 6b). Furthermore, Fig. 6c reveals that the EOF1-event frequency analysis made for the remaining models show an opposite behavior but not statistically significant (Fig. 6c).

In summary, the identified 9 models (CCCMA T43, CCCMA T63, CSIRO, GFDL2.0, GFDL2.1, MIROC hires, MIROC medres, MIUB, UKMO HadCM3), coherently exhibit: (1) a realistic representation of the dipole-like structure associated to EOF1 events in the present (Fig. 2) as in the future (not shown); (2) an increase of the projected summer rainfall in SESA by the end of the twenty first century and a decrease in the SACZ region (Fig. 3), accordingly with previous works (e.g., IPCC 2007; Vera et al. 2006b); and (3) an increase of the frequency of positive EOF1 events and a decrease of negative EOF1 events during the twenty first century (Fig. 6). These 9 models compose the multi-model ensemble used hereafter in our study.

In order to explore how much of the changes in the summer mean precipitation are accounted by changes in the activity of the dipole pattern EOF1, DJF rainfall changes between (2050–2098) and (2001–2049) were computed from the 9-model ensemble: (1) including only those years identified as positive and negative EOF1 events (Fig. 7a), (2) including complementary non-intense event years only (Fig. 7b), and (3) including all years (Fig. 7c).

Fig. 3 Differences of DJF mean precipitation between 2079–2999 and 1979–1999 periods simulated by the 18 models. *Color scale* interval is 0.2 mm day^{-1}. *Black contour* indicates the 0 level. The 9 models selected in Sect. 3.2 are marked in *red*
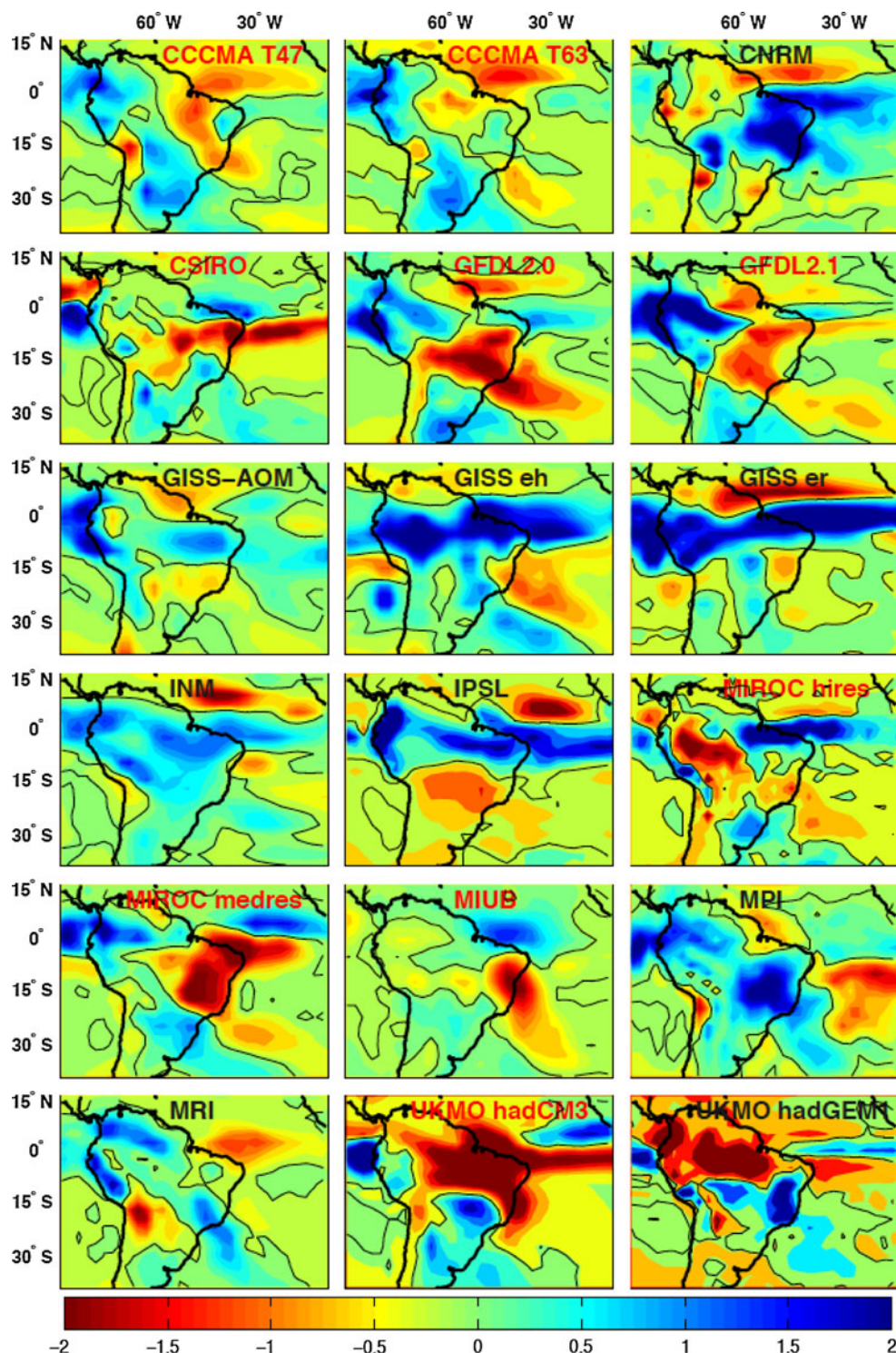
The three panels have been standardized by the total number of years so the last one corresponds to the sum of the two precedent ones. When EOF1 event years are only considered (Fig. 7a), DJF mean precipitation changes show a dipolar structure that contributes to an increase of mean precipitation in SESA and a decrease in the SACZ region. A comparison with Fig. 7c reveals that more than 70% of

the summer precipitation changes in SESA are explained by those summers associated to an active dipole EOF1. Such summers correspond roughly to a third of the total number of years. Figure 7b shows that rainfall changes associated to non-EOF1 event years also contribute to a generalized precipitation increase in the region but its contribution to rainfall increase in SESA is rather small
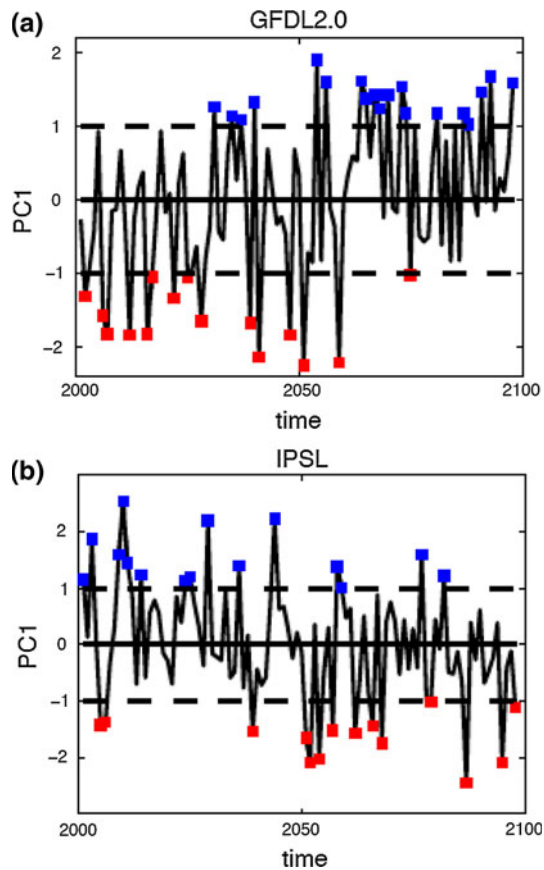
Fig. 4 Principal component (PC) of EOF1 for **a** GFDL2.0 and **b** IPSL models. *Blue* (*red*) *dots* mark positive (negative) EOF1 events identified by PC values exceeding 1(−1) of its interannual standard deviation, respectively
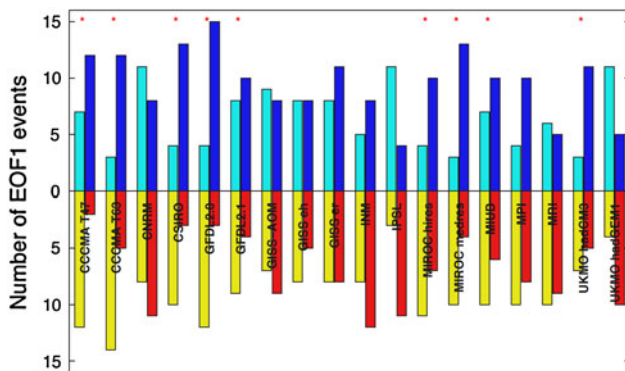

Fig. 5 Statistics of each individual model on the number of positive EOF1 events (*upper panel with light blue* for 2001–2049 and *dark blue* for 2050–2098) and on the number of negative EOF1 events (*lower panel with yellow* for 2001–2049 and *red* for 2050–2098). The 9 models selected in Sect. 3.3 are indicated with a *red star*

(less than 10%). We can conclude that projected summer rainfall changes in SESA are strongly related to changes in the activity of the dipole pattern depicted by EOF1, being the contribution from years associated to EOF1 events significantly larger than that from neutral years.
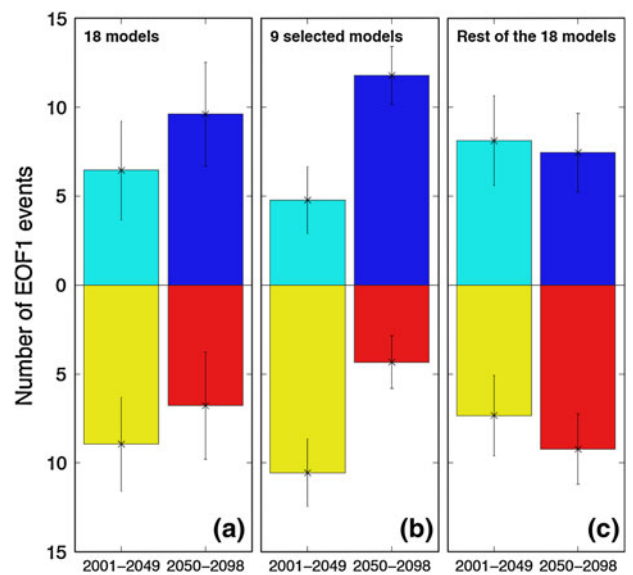
Fig. 6 Same as in Fig. 5, but in terms of ensemble-mean number. The *three panels* **a**, **b** and **c** represent respectively the ensemble mean of the 18 models, the 9 selected models and the rest. *Error bars* represent inter-model dispersion

The contribution of the EOF1-event changes to the positive trend of the summer precipitation projected in SESA was further explored. Figure 8 depicts the temporal evolution of the 9-model ensemble mean of DJF rainfall standardized anomalies and its corresponding linear trend over that particular region. Rainfall values were standardized before the 9-model ensemble mean computation, considering both mean and standard deviation values computed for each of the models over the whole period. Figure 8 also includes "the cloud" of standardized rainfall anomaly values associated to both positive and negative EOF1 events resulting from each of the 9 models. Besides the large dispersion observed among them, positive (negative) EOF1 events corresponding to DJF seasons with rainfall above- (below-) normal in SESA tend to be more frequent during the second (first) half of the twenty first century. Moreover, the positive trend (significant at $p < 0.01$) evident in the positive EOF1 events evolution aligns well with that described by the 9-model ensemble mean evolution, while that associated with the negative EOF1 events is not significant. In addition, it is noticeable that the 9-model ensemble mean seems to show two distinctive behaviors when the two halves of the twenty first century are separately considered: while the first half does not exhibit a significant rainfall trend, a positive trend (significant at $p < 0.01$) is clearly evident in the multi-model ensemble mean along the second part of the twenty first century (Fig. 8). This is in agreement with Hawkins and Sutton (2009) who showed that projections of regional climate change are largely influenced during the first half
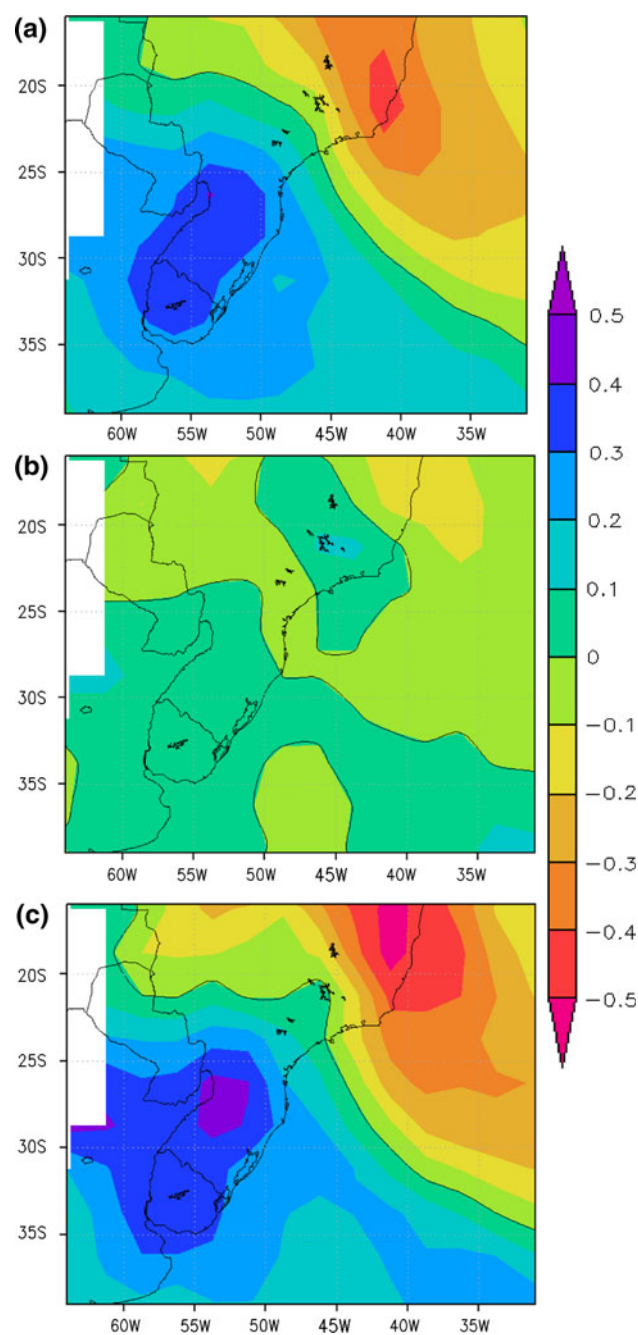
Fig. 7 Differences of mean DJF rainfall computed between 2050–2098 and 2001–2049 periods considering **a** Years associated to positive and negative EOF1 events, **b** Years not related to EOF1 activity, and **c** All years from the 9 selected models. The differences in the three panels are standardized by the total number of years. *Color scale* interval is 0.2 mm day^{-1}. *Black contour* indicates the 0 level
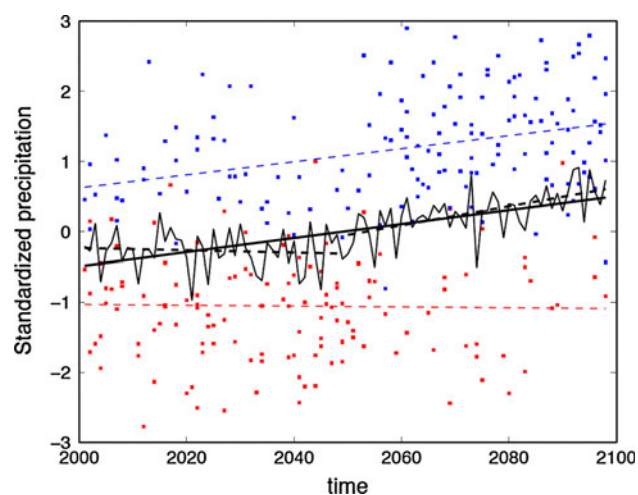
Fig. 8 Temporal evolution of the standardized DJF rainfall in SESA (38°S–26°S, 64°–50°W) from the 9-model mean during the twenty first century (*black thin line*) and its linear trend (*black thick line*). The rainfall linear trends for both the first and the second parts of the twenty first century are represented by the *two dashed black dashed thick lines. Blue* (*red*) *dots* correspond to the rainfall anomalies associated to each of the positive (negative) EOF1 events identified for each of the models (the corresponding linear trends are depicted in *dashed lines*)

We can conclude that the increase of rainfall in SESA by the end of the twenty first century seems associated to an increase of both frequency and intensity of the rainfall amounts promoted by positive phases of the rainfall dipole pattern. The evolution of the summers associated to the negative phase of the dipole is characterized by a decrease of their frequency but a quasi-constant evolution of their intensity.

4 Dynamics associated to rainfall dipole changes

The main dynamical features associated with the behavior of the dipole pattern, EOF1, in the context of a climate change is discussed in this section. The 9-model ensemble is used to compute composite fields of different variables. The fields are based on the ensemble mean of the composites computed from the positive and negative events of EOF1, identified for each of the models along the twenty first century. Those fields were also computed with the composites from each model standardized before the ensemble mean computation, and they resemble the same general structures (not shown).

4.1 SST

In order to explore the sources of the projected changes in EOF1 activity, we explored the SST anomaly patterns associated with both positive and negative EOF1 events.

of the twenty first century by uncertainties due to both natural variability and model differences while during the second half of the twenty first century climate change scenarios dominate the response.

Difference fields of SST anomaly composites between positive and negative EOF1 events are displayed in Fig. 9 for each half of the twenty first century. Two common regions of maximum positive SST anomalies are observed in both periods: the equatorial central Pacific, and the WSSA. This result is consistent with the studies cited in Introduction linking warm SST anomalies in both equatorial central Pacific and WSSA to positive phases of the DJF rainfall dipole. It is noticeable, however, that elsewhere of those two oceanic regions, global negative SST anomalies mainly characterize the composite differences for the first half of the twenty first century (Fig. 9a), while in the second half of the twenty first century the SST anomalies are mainly positive (Fig. 9b).

Changes in the intensity and spatial structural of the maximum positive SST anomaly centers were also observed between the first and the second parts of the twenty first century. During the first period, the maximum in WSSA is the dominant positive center (Fig. 9a), while that in the equatorial central Pacific becomes the main one during the second part of the twenty first century (Fig. 9b). During this last period, positive SST anomaly structure over the equatorial Pacific is more spatially extended while the SST anomaly center in WSSA is more spatially extended to the southwest. These changes are synthesized in Fig. 9c, which displays the difference of Fig. 9a, b. It is evident that changes in the rainfall dipole activity in SESA are associated to a generalized warming over most of the

Fig. 9 Composite differences of mean DJF SST anomalies between positive and the negative EOF1 events for
a (2001–2049), and
b (2050–2098) from the 9-model ensemble mean.
c Difference between **b** and **a**. *Color scale* interval is 0.2 K
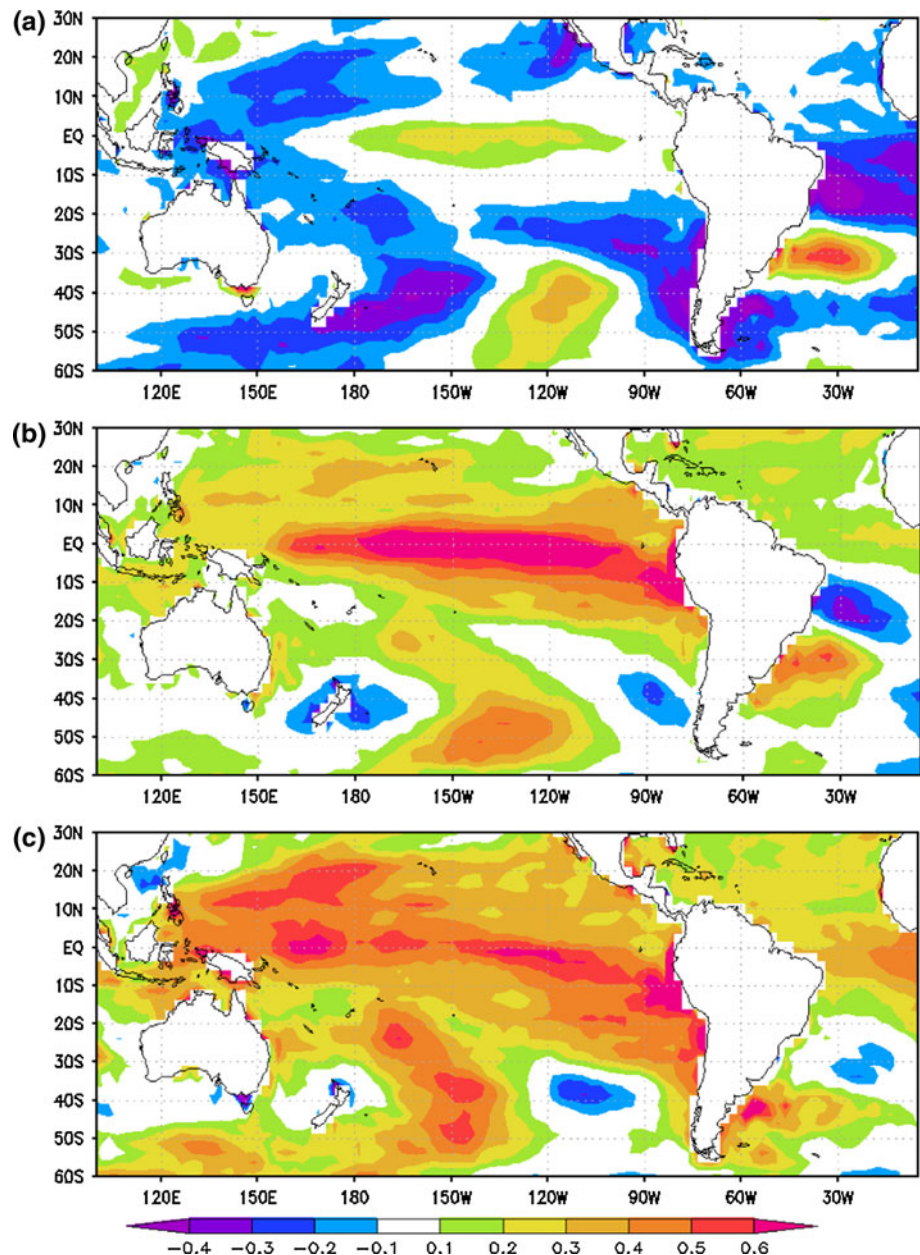
ocean regions, but being particularly larger in the equatorial central Pacific.

The temporal evolution of standardized SST anomalies in the equatorial central Pacific along the twenty first century in relationship to the activity of EOF1 dipole pattern is further explored. Figure 10a shows the evolution of the 9-model ensemble mean of the standardized DJF SST anomalies (spatially averaged over the box 6°S/6°N and 150/90°W) and its corresponding linear trend. SST values were standardized before the 9-model ensemble mean computation, considering both mean and standard deviation values computed over the whole period for each of the models. Figure 10a also includes the "cloud" of standardized SST anomalies associated to all EOF1 events identified for each of the 9 models. A large SST increase along the century dominates the evolution, as it is expected in a context of GHG increase scenario. However, it is still discernible that SST above (below) normal mainly related to positive (negative) EOF1 events are more frequent during the second (first) part of the twenty first century. Furthermore, the linear trend described by the SST anomalies related to positive (negative) EOF1 phases, is larger (smaller) than that resulted from the 9-model ensemble mean. These features are still evident when the positive linear trend is removed (Fig. 10b). Figure 11 shows the changes between the first and the second part of the twenty first century of the composite standardized SST anomalies in the equatorial central Pacific associated to both positive and negative EOF1 events as depicted by the 9-model ensemble mean. Standardized SST anomalies for both EOF1 phases exhibit a positive trend along the twenty first century that is significantly different from inter-model dispersion. In particular, the positive SST anomaly change associated to positive EOF1 events is 30% larger than that identified for the negative EOF1 events. It is also evident that for each half of the twenty first century, composite SST anomalies for positive EOF1 events are larger than those for negative events. Although, the composite SST anomaly differences between positive and negative EOF1 events are not significantly different from the inter-model variability, which provides some level of uncertainty to this result.

In summary, the activity of the rainfall dipole along the twenty first century in a context of GHG increase climate change scenario seems to be more influenced by the SST evolution in the equatorial central Pacific than in any other region. A positive (negative) EOF1 event is mainly characterized by SST above (below) normal over the equatorial Pacific. In addition, the evolution of both rainfall dipole phases along the twenty first century is associated with an intensity increase of warm SST anomalies in the equatorial Pacific. In particular, there is a tendency of the changes in the activity of the DJF rainfall dipole to prefer its positive
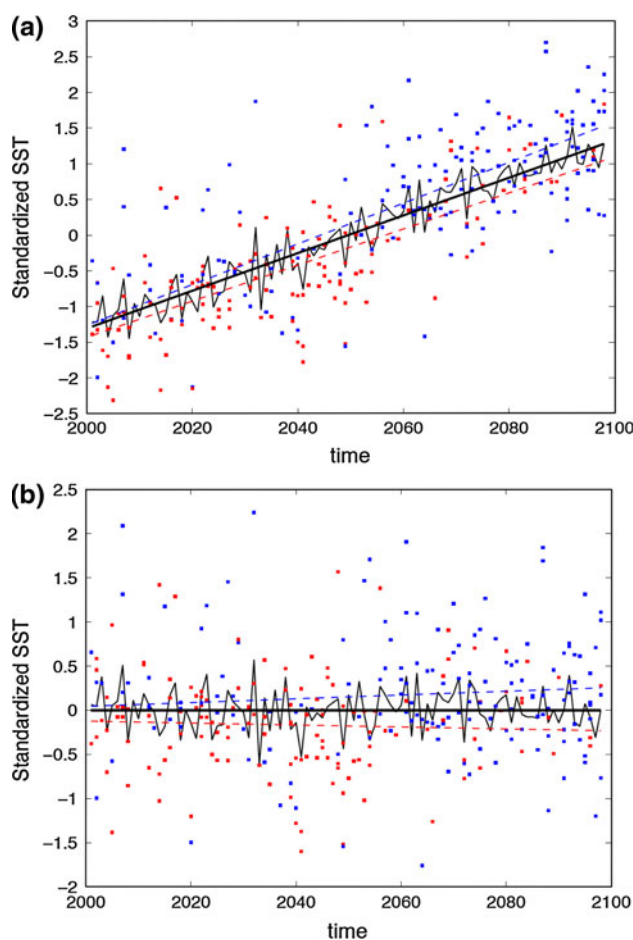

Fig. 10 a Temporal evolution of the standardized DJF SST in the equatorial central Pacific (6°S–6°N,150°W–90°W) from the 9-model mean during the twenty first century (*black thin line*) and its linear trend (*black thick line*). Blue (red) dots correspond to the standardized SST anomalies associated to each of the positive (negative) EOF1 events identified for each of the models (the corresponding linear trends are depicted in *dashed lines*). **b** Same as in a but for linearly detrended standardized SST anomalies

phase, in relationship to an increase of more intense equatorial Pacific positive SST anomalies by the second half of the twenty first century.

4.2 Atmospheric circulation changes

In order to better understand the links between the projected Pacific equatorial SST anomalies and EOF1 events changes, an analysis of the atmospheric circulation related pattern was made at both hemispheric and regional scales. In this particular study, only 7 of the selected 9 models were used due to the unavailability in the PCMDI dataset of some of the needed variables for MIUB and UKMO hadCM3 models.

The 500-hPa geopotential height composite difference between positive and negative EOF1 events, for the period
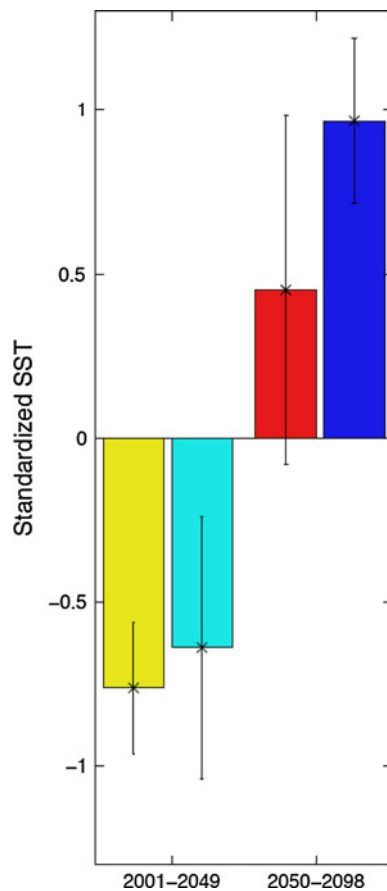
Fig. 11 Composites of standardized SST anomalies at the equatorial central Pacific (6°S–6°N,150°W–90°W) for positive (negative) EOF1 events, computed for 2001–2049 [*light blue* (*yellow*)], and for (2050–2098) [*dark blue* (*red*)] periods, from the 9-model ensemble mean. *Error bars* represent inter-model dispersion

2001–2049 is depicted in Fig. 12a. The circulation anomalies exhibit a wave train-like structure consisting of alternating positive and negative height-anomaly centers following an arch trajectory from the western tropical Pacific toward South America. A positive anomaly center is discernible over the SACZ region, while a negative anomaly center is evident at the southern tip of South America, which promotes favorable conditions for rainfall enhancement in SESA associated to positive EOF1 events. This pattern resembles the teleconnection that typically links SST anomalies in the equatorial Pacific with positive rainfall anomalies in SESA, in agreement with the previous works described in Introduction. During the second part of the twenty first century (Fig. 12b), a similar pattern is found, although the wave train structure is intensified, and the centers are displaced southwestward over South America and westward over the Pacific Ocean. It was found that such displacement is statistically significant over the south Pacific at the 90% level of a Student's *t* test (not shown).

The 850-hPa humidity flux composite differences between positive and negative EOF1 events, shows for both periods that the anticyclonic circulation anomaly observed in the SACZ region associated to positive EOF1 events (Fig. 12), favors moisture transport convergence in SESA and moisture divergence in the SACZ region (Fig. 13). This pattern agrees with those found by other studies and previously discussed (e.g., Nogués-Paegle and Mo 1997; Robertson and Mechoso 2000). The analysis of the changes of moisture transport composite differences between the two periods shows that the moisture transport convergence (divergence) anomaly center in SESA (SACZ) region is weakly displaced to the southwest (northwest) in the second half of the twenty first century (Fig. 13b), compared to their respective locations during the first half (Fig. 13a). In agreement, the corresponding composite maps for rainfall anomalies (Fig. 14) show that the dipole spatial structure is slightly shifted by the second part of the twenty first century, being the positive anomaly center in SESA displaced to the southwest while the negative anomaly center in the SACZ region is located toward the northwest.

Consequently, the analysis performed in this section confirms the presence of a teleconnection pattern linking the SST anomalies in the equatorial Pacific and the rainfall dipole in SESA. During positive EOF1 events, the Rossby wave train-like pattern extended along the South Pacific induces an anticyclonic anomaly circulation over tropical South America that enhances moisture convergence in SESA and reduces over the SACZ region. Results are consistent with previous studies describing the mechanisms associated to ENSO influence on rainfall variability in SESA. It was found that while these mechanisms are evident in both halves of the twenty first century, the structures are displaced between the first and the second half, resulting in a slight displacement of the rainfall dipole centers.

5 Summary and conclusion

Changes in the summer rainfall variability in SESA in the context of a global warming scenario associated to GHG increase were studied in this paper. Such changes were described in terms of the properties of the first leading pattern of rainfall variability in the region, characterized by a dipole-like structure with centers of action at both SESA and the SACZ region. The study was performed under the motivation in answering the following two main questions: how rainfall variability in SESA would change in a future climate and how much of that change explains the projected positive trends in the summer mean rainfall in SESA, identified in previous works.

Composite differences of DJF geopotential height anomalies at 500 hPa between positive and negative EOF1 events for **a** (2001–2049), and **b** (2050–2098) periods, computed from the 8-model ensemble mean. *Color scale* and contour interval is 10 m. Areas where values are statistically significant at the 90% of the Student test are inside a *black contour*
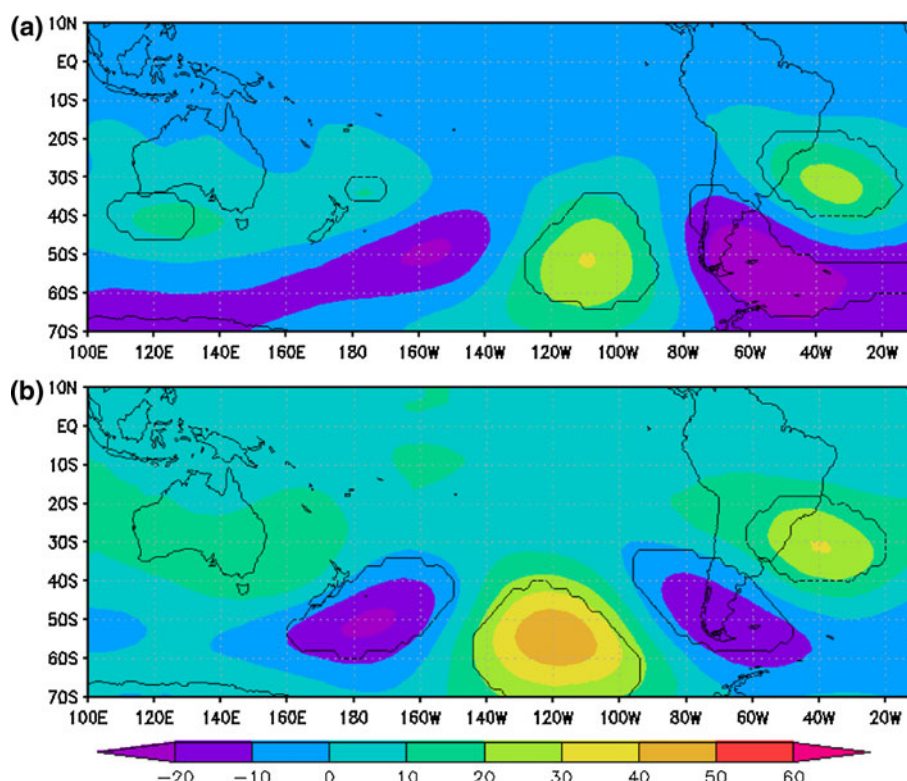
The study was based on the analysis of climate simulations of 18 climate models from the WCRP/CMIP3 dataset, for both current climate conditions and the SRES-A1B climate change scenario. The DJF rainfall dipole structure in SESA depicted by observations over the end of the twentieth century in association to the leading pattern of variability (EOF1) was found to be also the main intrinsic structure in the model simulations for both present and future climate conditions.

Changes in the EOF1 activity were described through the analysis of the frequency and intensity of both positive and negative EOF1 events, as defined by the corresponding principal component time series. Positive (negative) phases of EOF1 are associated to positive (negative) rainfall anomalies in SESA and negative (positive) anomalies in the SACZ region. Results obtained from the 18-model ensemble confirm that future rainfall variability in SESA has a strong projection on the changes of seasonal dipole pattern activity, being them associated to an increase of the frequency of DJF seasons associated to an EOF1 positive phase.

A detailed analysis of the EOF1 activity in a future climate was performed using 9 of the 18 models. The models were selected as those showing: (1) ability to represent the rainfall dipole pattern in the present as in the future climate, (2) coherence in projecting positive rainfall anomalies in SESA by the end of twenty first century, and (3) a coherent behavior of the future evolution of the dipole. The 9-model ensemble shows that the increase of

summer rainfall in SESA projected for the end of the twenty first century by most of the CGCMs, and already discussed in previous publications or summarized in IPCC (2007), seems to be associated with an increase (decrease) of the frequency of the positive (negative) events of the dipole leading pattern. Moreover, positive trend in DJF rainfall in SESA largely corresponds to a tendency of the rainfall dipole to prefer its positive phase. These results are in agreement with Silvestri and Vera (2008) that found an increase (decrease) in the frequency of heavy (low) summer rainfall by the end of the twenty first century at the southern and central portion of SESA.

Results also show that the frequency increase of positive dipole phase along the twenty first century seems to be associated to an increase of both frequency and intensity of positive SST anomalies in the equatorial Pacific. Furthermore, composites based on the 9-model ensemble outputs show a Rossby wave train-like anomaly pattern linking the equatorial Pacific to South America, which regionally induces favorable conditions for moisture transport convergence and rainfall increase in SESA, in agreement with previous works. A change of the structure of the dipole was also found by the second half of the twenty first century, characterized mainly by a southwestward displacement of the rainfall dipole center in SESA, together with the corresponding moisture transport convergence anomaly center, and a westward displacement of the Rossby wave pattern over the south Pacific.
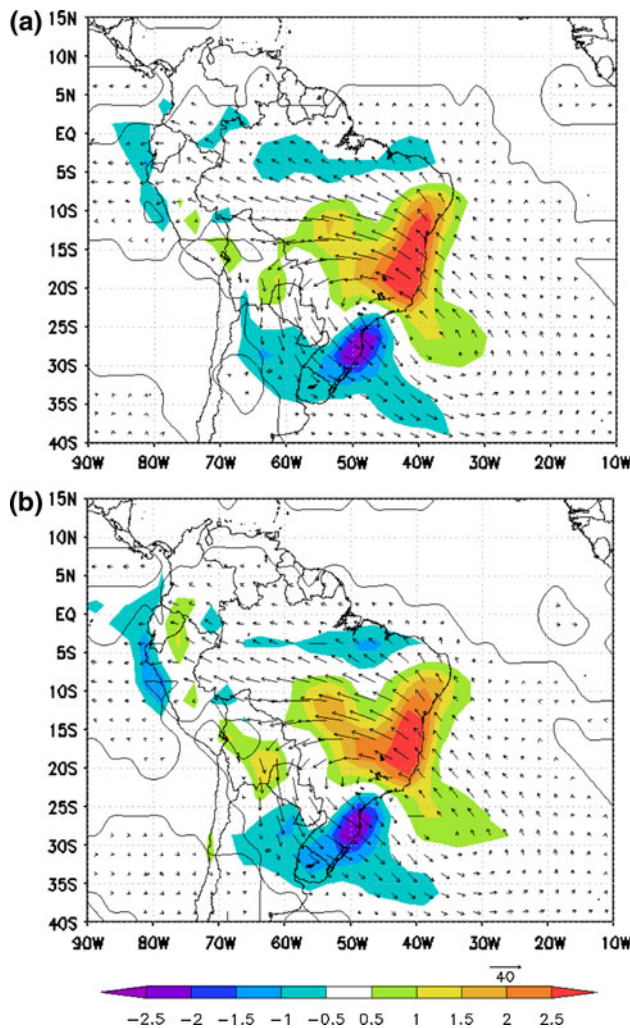
Fig. 13 Composite differences of moisture fluxes (*arrows*) and divergence (*contour*) at 850 hPa between positive and negative EOF1 events for **a** (2001–2049), and **b** (2050–2098) periods, computed from the 7-model ensemble mean. Positive (negative) values represent moisture divergence (convergence). Units: 10^5 g kg^{-1} s^{-1}. Reference vector of 40 g kg^{-1} m s^{-1} is displayed at the lower right corner. The zero contour is omitted. Areas where values are statistically significant at the 90% of the Student test are inside a *black contour*

In summary, this paper has shown that the positive summer rainfall changes projected in SESA by most of the WCRP/CMIP3 climate models in a context of global warming seems related to an increase of the frequency of summers influenced by warm conditions in the equatorial Pacific. It is important to point out that summer climate in SESA has generally been considered as weakly influenced by tropical Pacific SST anomalies as compared to the magnitude of that influence observed for other seasons like spring or fall (e.g., Grimm et al. 2000). However, the results of this paper show that future climate change seems to modify strongly the SST spatial structure for the tropical Pacific and thus its influence onto SESA climate variability.
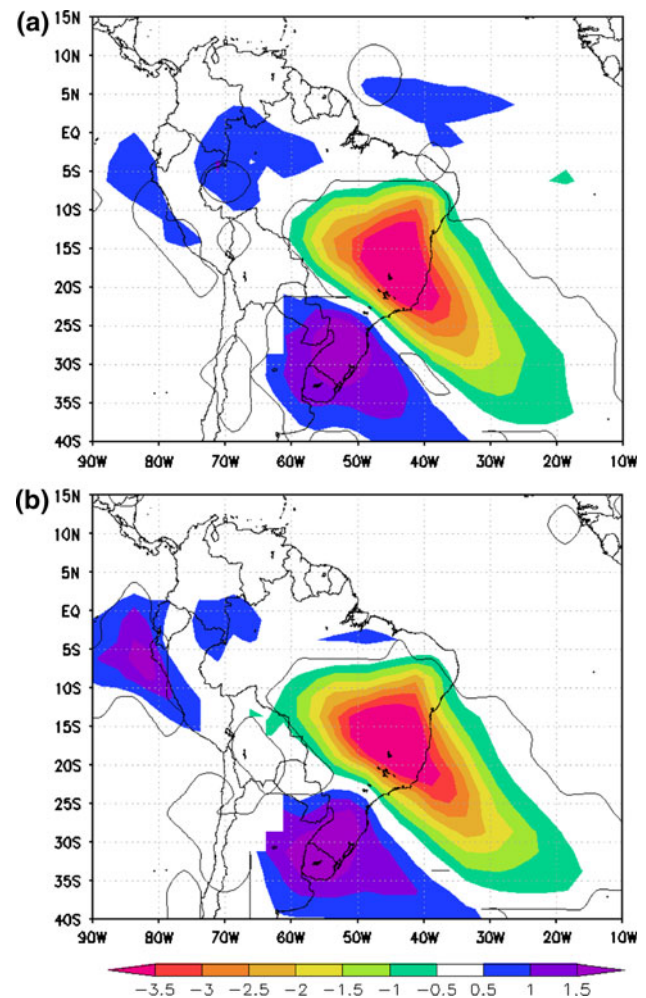

Fig. 14 Composite differences of DJF rainfall between positive and negative EOF1 events for **a** (2001–2049), and **b** (2050–2098) periods, computed from the 9-model ensemble mean. *Color scale* interval is 0.2 mm day^{-1}. The zero contour is omitted. Areas where values are statistically significant at the 90% of the Student test are inside a *black contour*

Such conclusion has been obtained from the analysis of a multi-model ensemble that includes some of the models that have also been identified by other studies among the "best" models in simulating present-day ENSO variability (GFDL2.1, MIROC hires, UKMO hadCM3, by van Oldenborgh et al. 2005; GFDL2.0, GFDL2.1 and UKMO hadCM3, by Guilyardi 2006). The same models have been identified by Vera and Silvestri (2009) as showing the better description of the hydroclimate features induced by ENSO in the Southern Hemisphere and regionally over South America. However, Leloup et al. (2008) identified 5 of our 9 models as displaying a tendency to have a stronger than observed maximum of SST anomalies variability in the western Pacific during ENSO. Moreover, the results described in Sect. 3.1, show that the percentage of variance explained by the EOF1 represented by the 9 models by the

end of the twentieth century is around 10% larger than that observed. Therefore, how much of the signal depicted by the CMIP3 climate change projections for the summer precipitation in SESA is related to the ability of current climate models in correctly reproducing both the tropical Pacific ocean dynamics and the associated teleconnection patterns, is not clear yet and should be focus of future researches.

References

Berbery EH, Barros V (2002) The hydrological cycle of the La Plata Basin in South America. J Hydrometeorol 3:630–645

Cerne B, Vera C (2010) Influence of the intraseasonal variability on heat waves in subtropical South America. Clim Dyn (in press)

Christensen JH, Hewitson B, Busuioc A, Chen A, Gao X, Held I, Jones R, Kolli RK, Kwon W-T, Laprise R, Magaña Rueda V, Mearns L, Menéndez CG, Räisänen J, Rinke A, Sarr A, Whetton P (2007) Regional climate projections. In: Solomon S, Qin D, Manning M, Chen Z, Marquis M, Averyt KB, Tignor M, Miller HL (eds) Climate change 2007: the physical science basis. Contribution of working group I to the fourth assessment report of the intergovernmental panel on climate change. Cambridge University Press, Cambridge, United Kingdom and New York, NY, USA

Delworth T et al (2006) GFDL's CM2 global coupled climate models—part 1: formulation and simulation characteristics. J Clim 19:643–674

Doyle ME, Barros VR (2002) Midsummer low-level circulation and precipitation in subtropical South America and related sea surface temperature anomalies in the South Atlantic. J Clim 15:3394–3410

Flato GM (2005) The third generation coupled global climate model (CGCM3) (and included links to the description of the AGCM3 atmospheric model). http://www.cccma.bc.ec.gc.ca/models/cgcm3.shtml

Gandu AW, Silva Dias PL (1998) Impact of tropical heat sources on the South American tropospheric upper circulation and subsidence. J Geophys Res 103:6001–6015

Giorgi F (2002) Variability and trends of sub-continental scale surface climate in the twentieth century. Part I: observations. Clim Dyn 18:675–691

Gordon C et al (2000) The simulation of SST, sea ice extents and ocean heat transports in a version of the Hadley Centre coupled model without flux adjustments. Clim Dyn 16:147–168

Gordon HB et al (2002) The CSIRO Mk3 climate system model. CSIRO Atmospheric Research Technical Paper No. 60. Commonwealth Scientific and Industrial Research Organisation Atmospheric Research, Aspendale, Victoria, Australia. http://www.cmar.csiro.au/e-print/open/gordon_2002a.pdf

Grimm A, Zilli MT (2009) Interannual variability and seasonal evolution of summer monsoon in South America. J Clim 22:2257–2275

Grimm A, Barros VR, Doyle ME (2000) Climate variability in southern South America associated with El Niño and La Niña events. J Clim 13:35–58

Guilyardi E (2006) El Niño-mean state-seasonal cycle interactions in a multi-model ensemble. Clim Dyn 26(4):329–348

Hasumi H et al (2004) K-1 coupled GCM (MIRCO) description. K-1 technical report no. 1, 34 pp. Available at http://www.ccsr.u-tokyo.ac.jp/kyosei/hasumi/MIROC/techrepo.pdf

Hawkins E, Sutton RT (2009) The potential to narrow uncertainty in regional climate predictions. Bull Am Meteorol Soc 90(8):1095–1107. ISSN 1520-0477

IPCC (2007) Summary for policymakers. In: Solomon S, Qin D, Manning M, Chen Z, Marquis M, Averyt KB, Tignor M, Miller HL (eds) Climate change 2007: the physical science basis. Contribution of working group I to the fourth assessment report of the intergovernmental panel on climate change. Cambridge University Press, Cambridge, United Kingdom and New York, NY, USA

Johns TC et al (2006) The new Hadley Centre climate model HadGEM1: evaluation of coupled simulations. J Clim 19:1327–1353

Jungclaus JH et al (2006) Ocean circulation and tropical variability in the AOGCM ECHAM5/MPI-OM. J Clim 19:3952–3972

Knutti R (2010) The end of model democracy? An editorial comment. Clim Chang 102:395–404

Kodama Y-M (1992) Large-scale common features of subtropical precipitation zones (the Baiu Frontal Zone, the SPCZ, and the SACZ). Part I: characteristics of subtropical frontal zones. J Meteorol Soc Jpn 70:813–835

Leloup J, Lengaigne M, Boulanger JP (2008) Twentieth century ENSO characteristics in the IPCC database. Clim Dyn 30:277–291

Li ZX, Le Treut H (1999) Transient behavior of the meridional moisture transport across South America and its relation to atmospheric circulation patterns. Geophys Res Lett 26:1409–1412

Marti O et al (2005) The new IPSL climate system model: IPSL-CM4. Note du Pôle de Modélisation No. 26. Institut Pierre Simon Laplace des Sciences de l'Environnement Global, Paris. http://dods.ipsl.jussieu.fr/omamce/IPSLCM4/DocIPSLCM4/FILES/DocIPSLCM4.pdf

Marengo JA, Liebmann B, Grimm AM, Misra V, Silva Dias PL, Cavalcanti IFA, Carvalho LMV, Berbery EH, Ambrizzi T, Vera CS, Saulo AS, Nogues-Paegle J, Zipser E, Seth A, Alves LM (2010) Recent developments on the South American monsoon system. Accepted in Int J Climatol

Meehl G, Covey C, Taylor KE, Delworth T, Stouffer RJ, Latif M, McAvaney B, Mitchell JFB (2007) THE WCRP CMIP3 multimodel dataset: a new era in climate change research. Bull Am Meteorol Soc 88:1383–1394

Min S-K, Legutke S, Hense A, Kwon W-T (2005) Climatology and internal variability in a 1000-year control simulation with the coupled climate model ECHO-G—I. Near-surface temperature, precipitation and mean sea level pressure. Tellus 57A:605–621

Nakicenovic N et al (2000) Special Report on Emissions Scenarios. In: Nakicenovic N, Swart R (eds) Cambridge Univ Press, New York

Nogués-Paegle J, Mo K (1997) Alternating wet and dry conditions over South America during summer. Mon Weather Rev 125:279–291

Paegle JN, Mo KC (2002) Linkages between summer rainfall variability over South America and sea surface temperature anomalies. J Clim 15:1389–1407

Robertson AW, Mechoso CR (2000) Interannual and interdecadal variability of the South Atlantic convergence zone. Mon Weather Rev 128:2947–2957

Rodwell MR, Hoskins BJ (2001) Subtropical anticyclones and summer monsoons. J Clim 14:3192–3211

Russell GL (2005) 4×3 atmosphere-ocean model documentation. http://aom.giss.nasa.gov/doc4x3.html

Salas-Melia D, Chauvin F, Deque M, Douville H, Gueremy J, Marquet P, Planton S, Royer J, Tyteca S (2005) Description and validation of the CNRM-CM3 global coupled model. CNRM working note 103

Schmidt GA et al (2006) Present day atmospheric simulations using GISS ModelE: comparison to in situ, satellite and reanalysis data. J Clim 19:153–192. http://www.giss.nasa.gov/tools/modelE/

Silvestri G, Vera C (2008) Evaluation of the WCRP-CMIP3 model simulations in the La Plata Basin. Meteorol Appl 15:497–502

van Oldenborgh G, Philip S, Collins M (2005) El Niño in changing climate: a multi-model study. Ocean Sci 1:81–95

Vera C, Silvestri G (2009) Precipitation interannual variability in South America from the WCRP-CMIP3 multi-model dataset. Clim Dyn 32:1003–1014

Vera CS et al (2006a) Toward a unified view of the American monsoon systems. J Clim 19:4977–5000, WN: 0628807462003

Vera CS, Silvestri G, Liebmann B, Gonzalez P (2006) Climate change scenarios for seasonal precipitation in South America from IPCC-AR4 models. Geophys Res Lett 33:L13707. doi:10.1029/2006GL025759

Volodin EM, Diansky NA (2004) El-Niño reproduction in a coupled general circulation model of atmosphere and ocean. Russ Meteorol Hydrol 12:5–14

Xie P, Arkin PA (1997) Global precipitation: a 17-year monthly analysis based on gauge observations, satellite estimates, and numerical model outputs. Bull Am Meteorol Soc 78:2539–2558

Yukimoto S et al (2006) Present-day climate and climate sensitivity in the Meteorological Research Institute Coupled GCM, Version 2.3 (MRI-CGCM2.3). J Meteorol Soc Jpn 84:333–363